

# On-chip sampling of optical fields with attosecond resolution

**Mina Bionta** (✉ [mbionta@mit.edu](mailto:mbionta@mit.edu))

Massachusetts Institute of Technology <https://orcid.org/0000-0003-0573-5375>

**Felix Ritzkowski**

DESY

**Marco Turchetti**

Massachusetts Institute of Technology

**Yujia Yang**

Massachusetts Institute of Technology <https://orcid.org/0000-0003-1524-7973>

**Dario Cattozzo Mor**

Massachusetts Institute of Technology

**William Putnam**

University of California, Davis <https://orcid.org/0000-0002-4901-461X>

**Franz Kärtner**

Deutsches Elektronen-Synchrotron - DESY

**Karl Berggren**

Massachusetts Institute of Technology <https://orcid.org/0000-0001-7453-9031>

**Phillip Keathley**

Massachusetts Institute of Technology <https://orcid.org/0000-0003-1325-1768>

---

## Article

**Keywords:** on-chip sampling, optoelectronic device sampling, attosecond resolution, nanoantennas

**Posted Date:** November 11th, 2020

**DOI:** <https://doi.org/10.21203/rs.3.rs-90476/v1>

**License:**  This work is licensed under a Creative Commons Attribution 4.0 International License.

[Read Full License](#)

---

**Version of Record:** A version of this preprint was published at Nature Photonics on April 15th, 2021. See the published version at <https://doi.org/10.1038/s41566-021-00792-0>.

# On-chip sampling of optical fields with attosecond resolution

Mina R. Bionta<sup>1,†,\*</sup>, Felix Ritzkowski<sup>2,†,\*</sup>, Marco Turchetti<sup>1,†</sup>, Yujia Yang<sup>1</sup>, Dario Cattozzo Mor<sup>1</sup>, William P. Putnam<sup>3</sup>, Franz X. Kärtner<sup>2</sup>, Karl K. Berggren<sup>1</sup>, and Phillip D. Keathley<sup>1,\*</sup>

<sup>1</sup>Research Laboratory of Electronics, Massachusetts Institute of Technology, 77 Massachusetts Avenue, Cambridge, MA 02139, USA

<sup>2</sup>Deutsches Elektronen Synchrotron (DESY) & Center for Free-Electron Laser Science, Notkestraße 85, 22607 Hamburg, Germany

<sup>3</sup>Department of Electrical and Computer Engineering, University of California, Davis, 1 Shields Ave, Davis, CA 95616, USA

<sup>†</sup>These authors contributed equally to this work.

\*e-mail: mbionta@mit.edu; felix.ritzkowski@desy.de; pdkeat2@mit.edu

## Abstract

We demonstrate an on-chip, optoelectronic device capable of sampling arbitrary, low-energy, near-infrared waveforms under ambient conditions with sub-optical-cycle resolution. Our detector uses field-driven photoemission from resonant nanoantennas to create attosecond electron bursts that probe the electric field of weak optical waveforms. Using these devices, we sampled the electric fields of  $\sim 5$  fJ ( $6.4 \text{ MV m}^{-1}$ ), few-cycle, near-infrared waveforms using  $\sim 50$  pJ ( $0.64 \text{ GV m}^{-1}$ ) near-infrared driving pulses. Beyond sampling these weak optical waveforms, our measurements directly reveal the localized plasmonic dynamics of the emitting nanoantennas *in situ*. Applications include broadband time-domain spectroscopy of molecular fingerprints from the visible through the infrared, time-domain analysis of nonlinear phenomena, and detailed investigations of strong-field light-matter interactions.

## Main

Time-domain sampling of arbitrary electric fields with sub-cycle resolution enables complementary time-frequency analyses of a system's electromagnetic response. Such time-frequency analyses provide dynamic information that is not furnished by absorption spectra alone. Accordingly, sub-cycle, time-domain sampling has proven critical to the understanding and design of electronic systems, and has revolutionized spectroscopy in the terahertz spectral region<sup>1,2</sup>. Commercial THz time-domain spectroscopy systems are now readily available and often used for industrial applications such as chemical and material analysis.

1 Sub-cycle field sampling in the THz regime has also been instrumental to many fundamental scientific in-  
2 vestigations, including the tracing of electron wavepacket dynamics in quantum wells<sup>3</sup>, the investigation  
3 of dynamic Bloch oscillations in semiconductor systems<sup>4</sup>, the observation and characterization of quantum  
4 vacuum fluctuations<sup>5</sup>, and other nonlinear phenomena<sup>6</sup>.

5 If readily available, sub-cycle optical-field sampling in the visible to near-infrared (near-IR) spectral re-  
6 gions would likewise provide great benefit to both science and industry. For example, attosecond streaking  
7 spectroscopy has been used to study the role of optical-field-controlled coherent electron dynamics in the  
8 control of chemical reaction pathways<sup>7</sup> and to investigate petahertz-level electrical currents in solid-state  
9 systems<sup>8-10</sup>. It was also recently shown that sub-cycle field sampling of the free-induction decays of biolog-  
10 ical systems can provide an order of magnitude reduction in the limits of detection and improved molecular  
11 sensitivity compared to traditional frequency-domain spectroscopic methods<sup>11</sup>. Despite these compelling re-  
12 sults, scaling such techniques into the near-IR and visible spectral regions has remained challenging. While  
13 the manipulation of attosecond electron wave packet emission<sup>10,12,13</sup> and attosecond streaking in the vis-  
14 ible to near-IR spectral regions<sup>14-16</sup> have proven to be viable paths towards direct optical-field sampling  
15 in the time-domain, these techniques are seldom accessible, requiring large driving pulse energies, and ac-  
16 cordingly, large laser amplifier systems, bulky apparatuses, and in some cases vacuum environments<sup>10-12,17</sup>.  
17 Currently, there is no compact and integratable sub-cycle optical field sampling technology with the band-  
18 width and field sensitivity required for real-world applications of interest in the visible to near-IR spectral  
19 regions.

20 To address this lack of compact and integratable tools for optical-field sampling in the visible to near-IR,  
21 we have developed and demonstrated an on-chip, sub-optical-cycle sampling technique for measuring arbi-  
22 trary electric fields of few-fJ near-IR optical pulses in ambient conditions. To our knowledge, this represents  
23 an improvement of roughly six orders of magnitude in energy sensitivity relative to the current state of the  
24 art. Our work leverages the sub-cycle optical-field emission from plasmonic nanoantennas<sup>18-22</sup> to achieve  
25 petahertz-level sampling bandwidths using only picojoules of energy<sup>23-26</sup>. Furthermore, by electrically con-  
26 necting the nanoantenna arrays via nanoscale wires, the field samplers we demonstrate here are amenable  
27 to large-scale electronic integration<sup>27,28</sup>. Beyond demonstrating the feasibility of sub-cycle field sampling  
28 of petahertz-scale frequencies, our results also reveal *in situ* dynamical properties of the interaction of the  
29 driving optical-field waveform with the plasmonic nanoantennas. This work will enable the development of  
30 new tools for optical metrology that will complement traditional spectroscopic methods and unravel linear

1 and nonlinear light-matter interactions as they occur at their natural time and length scales.

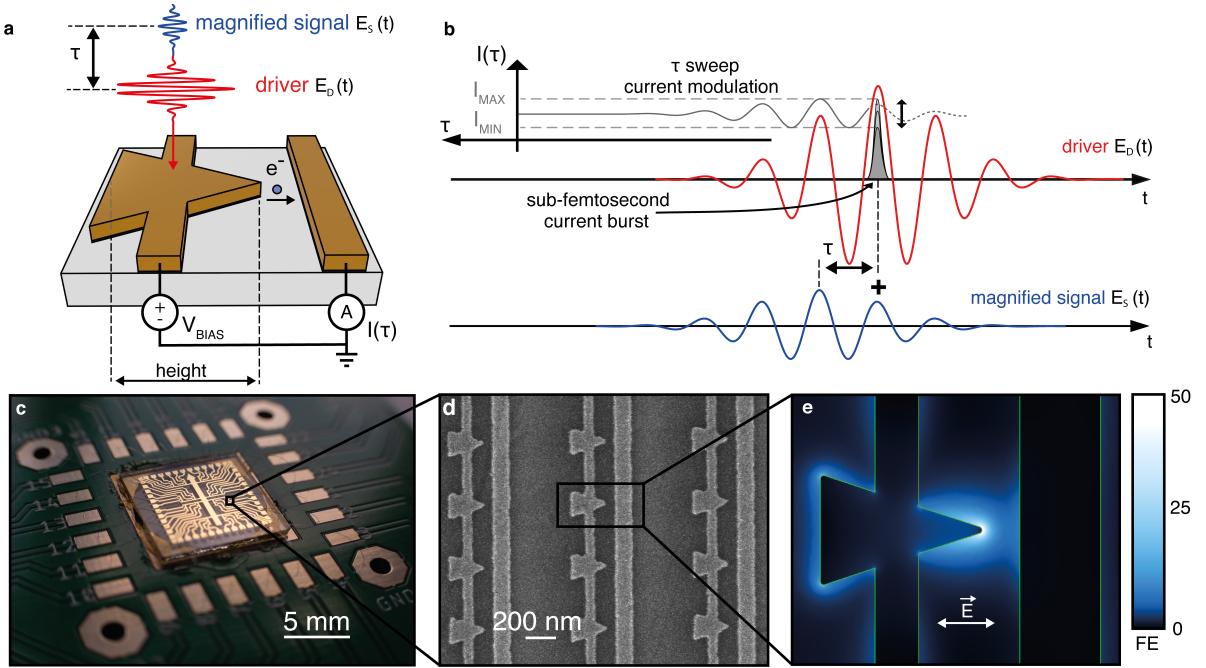


Figure 1. **Device overview.** **a**, Schematic of the device. **b**, Depiction of the optical-field sampling process. Attosecond electron bursts are driven from an electrically-connected gold nanoantenna (see **a**) by a strong optical waveform driver ( $E_D(t)$ , red), collected by an adjacent gold wire, then measured using an external current detector (see Methods). The weak signal waveform ( $E_S(t)$ , blue), with a peak intensity of  $1 \times 10^{-4}$  that of the driver pulses, modulates the average photocurrent generated by the driver pulse,  $I(\tau)$ , as a function of delay,  $\tau$  (grey). The amplitude of the signal waveform is artificially magnified in **a** and **b** for visibility. **c**, Photograph of the nanocircuit embedded on printed circuit board. **d**, Scanning electron micrograph of the device. **e**, Simulated electric field enhancement around a nanoantenna. The maximum field enhancement is  $\sim 35$ . FE: field enhancement factor. E: polarization direction of the incident electric field.

2 Our device is depicted in Fig. 1a. It consists of an electrically-connected plasmonic gold nanoantenna that  
 3 functions as the electron source (cathode), a gold nanowire as an anode separated by a 50 nm air gap, and an  
 4 external current detector. A photograph of the nanocircuit integrated onto a printed circuit board is shown  
 5 in Fig. 1c. Devices were connected in parallel via nanowires and simultaneously excited to improve signal  
 6 strength. A scanning electron micrograph (SEM) of the fabricated devices is shown in Fig. 1d.

7 When a strong driving pulse  $E_D(t)$  illuminates the nanoantenna/wire junction, a large local electric field  
 8  $E_D^{(L)}(t)$  is generated at the nanoantenna tip as shown in Fig. 1e. This incident electric field  $E_D(t)$  is re-  
 9 lated to  $E_D^{(L)}(t)$  by the transfer function of the nanoantenna  $\tilde{H}_{Pl.}(\omega)$  given by the relationship  $E_D^{(L)}(t) =$

1  $\mathcal{F}^{-1}(\tilde{H}_{\text{Pl.}}(\omega) \cdot \tilde{E}_{\text{D}}(\omega))$ , where  $\mathcal{F}^{-1}$  is the inverse Fourier transform, and tildes indicate the frequency do-  
 2 main. Due to the combined effect of the localized surface plasmon polariton<sup>22</sup> in the antenna and the geo-  
 3 metric field enhancement resulting from the sharp radius of curvature<sup>29</sup>, the locally-enhanced field exceeds  
 4 the incident electric field of the driver pulse by a factor of  $\sim 35$  (Fig. 1a). If sufficiently strong,  $E_{\text{D}}^{(\text{L})}(t)$   
 5 significantly bends the surface potential, resulting in optical-field-driven tunneling of electrons at the metal-  
 6 vacuum interface once every cycle<sup>24,25,27,30</sup>. Due to the strong nonlinearity of the emission process, the  
 7 electron bursts generated in the device are deeply sub-cycle and on the order of several hundred attoseconds  
 8 for the case of near-IR fields<sup>23,25</sup>. The weak incident signal field  $E_{\text{S}}(t)$  is similarly modified to create a weak  
 9 local signal field  $E_{\text{S}}^{(\text{L})}(t)$ , but remains too weak to drive photoemission.

10 As demonstrated by Cho *et al.*<sup>13</sup>, a short optical driving pulse in combination with a highly-nonlinear,  
 11 sub-cycle emission process allows for field-resolved sampling of the signal pulse. For calculating the impact  
 12 of  $E_{\text{S}}(t)$ , on the total emission, a linearized small-signal model can be used. Consider the addition of  $E_{\text{S}}^{(\text{L})}(t)$   
 13 as a function of delay  $\tau$  relative to the strong driving field  $E_{\text{D}}^{(\text{L})}(t - \tau)$  as shown in Fig. 1b. In our case, the  
 14 detected current as a function of delay  $I(\tau)$  is the time-average of the nonlinear emission rate  $\Gamma$ <sup>31,32</sup> driven  
 15 by the sum of the driver field  $E_{\text{D}}^{(\text{L})}(t)$  and the small-amplitude signal field  $E_{\text{D}}^{(\text{L})}(t - \tau)$ ,

$$I(\tau) \propto \int_{-\frac{T_{\text{Rep.}}}{2}}^{\frac{T_{\text{Rep.}}}{2}} \Gamma(E_{\text{D}}^{(\text{L})}(t - \tau) + E_{\text{S}}^{(\text{L})}(t)) dt, \quad (1)$$

16 where  $T_{\text{Rep.}}$  is the time between consecutive optical pulses. Given that  $E_{\text{S}}^{(\text{L})}(t)$  is sufficiently small, we can  
 17 Taylor-expand  $\Gamma$  around the local driver field  $E_{\text{D}}^{(\text{L})}(t - \tau)$  to the first order. This enables the linearization of  
 18 the measured emission  $I(\tau)$  with respect to the signal  $E_{\text{S}}^{(\text{L})}(t)$ :

$$I(\tau) \propto \int_{-\frac{T_{\text{Rep.}}}{2}}^{\frac{T_{\text{Rep.}}}{2}} \left( \Gamma(E_{\text{D}}^{(\text{L})}(t - \tau)) + \left. \frac{d\Gamma}{dE} \right|_{E_{\text{D}}^{(\text{L})}(t - \tau)} \cdot E_{\text{S}}^{(\text{L})}(t) \right) dt. \quad (2)$$

19 The second term in equation (2) is a cross-correlation between  $\left. \frac{d\Gamma}{dE} \right|_{E_{\text{D}}^{(\text{L})}(t - \tau)}$  and  $E_{\text{S}}^{(\text{L})}(t)$ , and denoted as  
 20  $I_{\text{CC}}(\tau)$ . Due to the nonlinearity of the emission process, the central most portion of the driving waveform  
 21 dominates the measured time-integrated current, and acts a sub-cycle gate limiting interaction with the signal  
 22 field (Fig. 2a inset). This fact becomes more evident when taking the Fourier transform of  $I_{\text{CC}}(\tau)$ , which

1 simplifies to the following expression:

$$\tilde{I}_{CC}(\omega) \propto \mathcal{F} \left( \left. \frac{d\Gamma}{dE} \right|_{E_D^{(L)}(t)} \right)^* \cdot \tilde{E}_S^{(L)}(\omega), \quad (3)$$

2 where  $\mathcal{F} \left( \left. \frac{d\Gamma}{dE} \right|_{E_D^{(L)}(t)} \right)^*$  is the complex spectrum shown in Fig. 2a and is denoted as  $\tilde{H}_{Det}(\omega)$ . This function

3  $\tilde{I}_{CC}(\omega)$  describes the full sampling response to the weak signal.

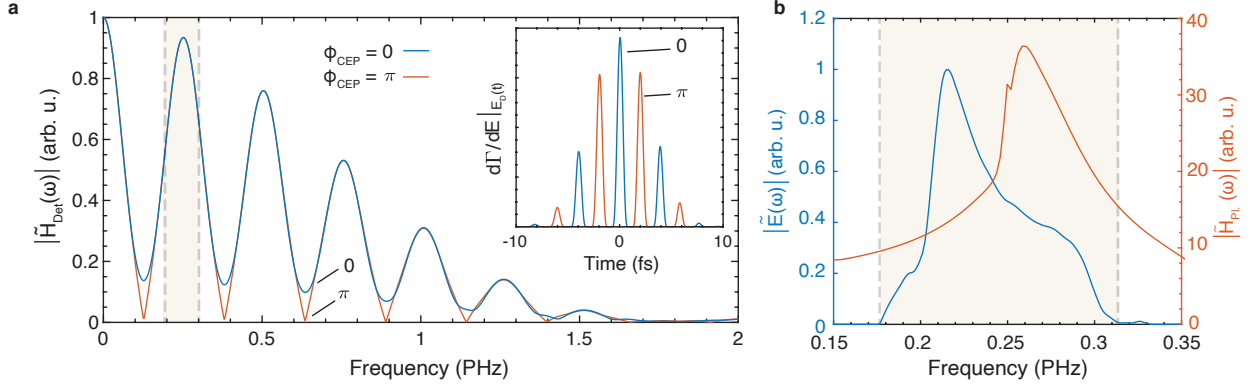


Figure 2. **Theoretical sampling bandwidth.** **a**, Calculation of the accessible sampling bandwidth  $\tilde{H}_{Det}(\omega)$  for the carrier-envelope phases  $\Phi_{CEP} = 0, \pi$  of the driver pulse (blue and red respectively). (Inset) The time-domain picture of  $\left. \frac{d\Gamma}{dE} \right|_{E_D(t)}$  corresponding to the bandwidth shown in **a**. **b**, The spectral amplitude of the driving pulse ( $E_D(t)$ , blue) and the plasmonic nanoantenna transfer function  $|\tilde{H}_{Pl}(\omega)|$  (red). The shaded area in **a** and **b** indicates the spectral region occupied by the driving pulse.

4 Multiplying the initial small signal  $\tilde{E}_S^{(L)}(\omega)$  with  $\tilde{H}_{Det}(\omega)$  gives the accessible bandwidth of the device,  
5 which, due to the highly-nonlinear sub-cycle response of the emission rate on the driving electric field, spans  
6 several octaves from DC to more than 1 PHz (see Fig. 2a). The resultant small-signal gain enhances the  
7 response of the system to the weak signals of interest  $\tilde{E}_S^{(L)}(\omega)$  that would not be able to generate detectable  
8 electron emission signals on their own. We should also note the periodic structure in the plot of  $\tilde{H}_{Det}(\omega)$   
9 shown in Fig. 2a is due to the presence of regularly-spaced electron pulses in the time domain modulating  
10 the amplitude of  $\tilde{H}_{Det}(\omega)$  (see inset of Fig. 2a). These pulses are spaced by one cycle of the driving laser,  
11 and change in number and strength depending on the carrier-envelope phase (CEP). However, for few-cycle  
12 pulses, such as those used in this experiment, the response remains relatively flat over the bandwidth of the  
13 driving pulse, and is only minimally affected by the modulation. More detailed discussion of CEP and pulse  
14 duration effects can be found in the Supplementary Information Sec. S2 and S3.

1 To experimentally verify the device performance, a CEP-stable, 78 MHz Er: fiber-based laser source was  
 2 used<sup>33</sup>, with a pulse duration of  $\sim 10$  fs full-width at half-maximum (FWHM) ( $\sim 2.5$  cycles) and central  
 3 wavelength of  $\sim 1170$  nm, locked to a fixed CEP. Laser pulse characterization can be found in Supplementary  
 4 Information Sec. S6. A dispersion-balanced Mach-Zehnder interferometer was used to generate pairs of  
 5 strong driver and weak signal pulses with a variable delay for the experiment. The driver and signal pulse  
 6 energies (fields) were measured to be approximately 50 pJ ( $0.64$  GV  $\text{m}^{-1}$  at focus) and  $\sim 5$  fJ ( $6.4$  MV  $\text{m}^{-1}$   
 7 at focus) respectively. The two pulses were focused to a spot-size of  $2.25 \mu\text{m} \times 4.1 \mu\text{m}$  FWHM, illuminating  
 8 10-15 nanoantennas at a time. The pulses were linearly polarized along the height axis of the nanoantennas  
 9 (Fig. 1e). Attosecond electron bursts were generated in the nanocircuit by the 50 pJ driver pulse, modulated  
 10 by the 5 fJ signal pulse as the delay between the two pulses was scanned. The signal pulses, with an intensity  
 11 of  $1 \times 10^{-4}$  that of the driver pulses, were much too weak to drive photoemission. The photocurrent was  
 12 then detected using a transimpedance amplifier in conjunction with lock-in detection. We emphasize that the  
 13 experiment was performed in ambient conditions (*i.e.* in air and at room temperature). A schematic of the  
 14 experiment is shown in Fig. 1a and Supplementary Fig. S1 with further details found in the Methods section  
 15 and Supplementary Information Sec. S1.

## 16 Results and Discussion

17 Fig. 3 presents the measured cross-correlation  $I_{\text{CC}}(\tau)$  (blue trace) for the tested antennas with a 240 nm  
 18 height (from antenna base to tip, see Fig. 1a), and compares it to the computed simulated antenna response  
 19  $E_{\text{S}}^{(\text{L})}(t)$  (red trace) and the calculated laser signal  $E_{\text{S}}(t)$  (yellow trace), found by applying the measured spec-  
 20 tral phase (see Supplementary Information Sec. S6) of the laser output to the measured intensity spectrum  
 21 before converting back to the time domain. The  $1\sigma$ -confidence interval (that is the interval ranging between  
 22 plus and minus one standard deviation from the mean value) was calculated over all 60 scans and is shown as  
 23 the light blue shaded region in Fig. 3. One standard deviation is  $\approx 10\%$  of the peak amplitude. Considering  
 24 the estimated peak field of around  $6.4$  MV  $\text{m}^{-1}$  for the incident laser signal, the detection floor is estimated  
 25 around  $640$  kV  $\text{m}^{-1}$ . The measured trace (blue) shows significant deviations from  $E_{\text{S}}(t)$  (yellow), especially  
 26 in the pedestal from 5 fs to 20 fs. However, this measured pulse shape in the time domain (blue trace) is  
 27 almost identical to  $E_{\text{S}}^{(\text{L})}(t)$  (red trace), both with a  $180^\circ$  dephasing near 12 fs with respect to  $E_{\text{S}}(t)$  (yel-  
 28 low trace). Similar dephasing dynamics have been investigated by others in both nanoantenna and extended  
 29 nanotip structures<sup>34</sup> and are a hallmark of the resonant electron dynamics excited within the nanoantennas.

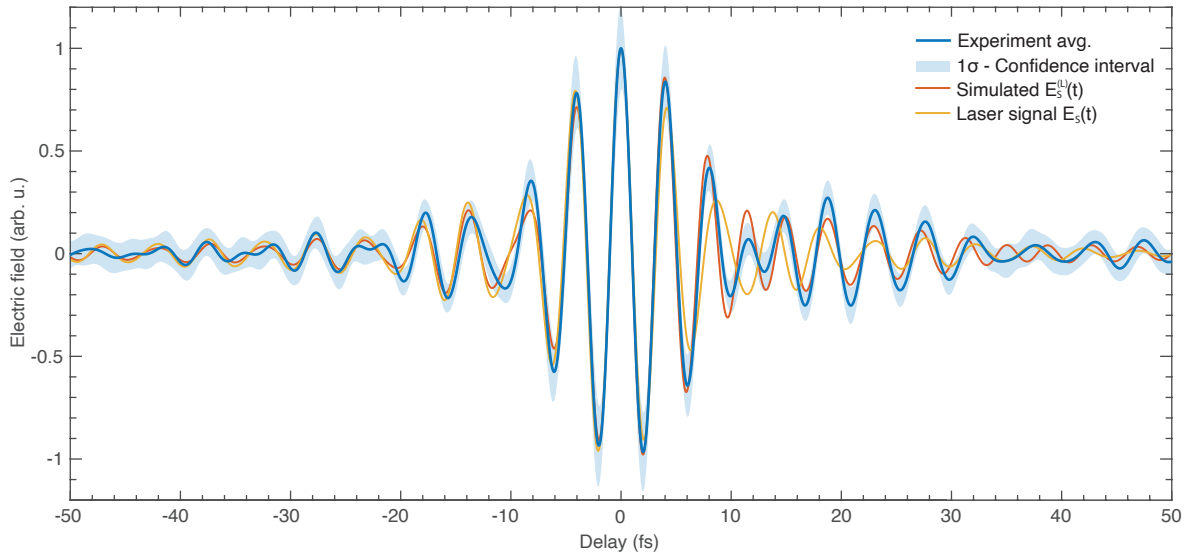


Figure 3. **Experimental field sampling results and analysis.** Time-domain results for devices with a height of 240 nm comparing measured (blue) and simulated near-fields ( $E_S^{(L)}(t)$ , red) to the calculated incident laser signal ( $E_S(t)$ , yellow). Negative delays indicate that the driver pulse arrives before the signal pulse. The  $1\sigma$ -confidence interval is shown as a blue shaded ribbon centered around the average value (blue solid line) retrieved from 60 scans. The plasmonic resonance of the antenna results in the dephasing in the time-domain between  $E_S(t)$  and  $E_S^{(L)}(t)$  observed around 12 fs.

1 In the frequency domain (Fig. 4), two prominent maxima are visible in the Fourier transform of the  
 2 measured data (blue solid trace). These maxima are also exhibited in the simulation of the antenna response  
 3 ( $\tilde{E}_S^{(L)}(\omega)$ , light blue dashed trace), but only one (at 218 THz) is observed in the measured laser spectrum  
 4 ( $\tilde{E}_S(\omega)$ , grey dotted trace). The second peak (at 257 THz) is due to the plasmonic response of the antenna  
 5  $\tilde{H}_{Pl}(\omega)$  which must be incorporated when calculating the electric near-field. The peak in the spectral phase  
 6 of the measured data (red solid trace) is due to the plasmonic resonance of the antenna and closely matches  
 7 the simulation of the antenna response (orange dashed trace). This spectral analysis further supports our  
 8 conclusion that the observed discrepancies and dephasing between the incident laser signal  $E_S(t)$  and the  
 9 measured pulse in the time-domain (Fig. 3) arise due to the resonant response of the nanoantenna. Similar  
 10 experimental results and analysis for 200 nm devices can be found in Supplementary Information Sec. S4.

11 There are several practical considerations for sampling incident signal fields with such a detector. In our  
 12 experimental data, we attribute the minor discrepancies with the the simulated model to slight uncertainties  
 13 in the fabrication process, as well as to the multiplexed nature of our current detection scheme. As we illu-

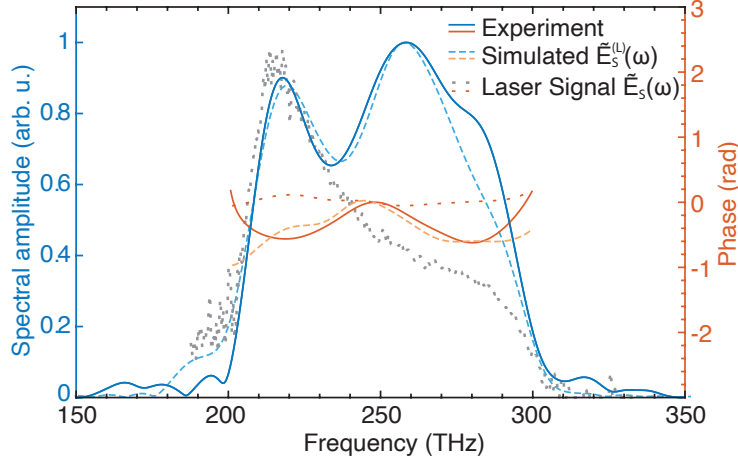


Figure 4. **Frequency-domain of the experimental field sampling results** Frequency-domain comparison of measured (solid) and simulated ( $\tilde{E}_S^{(L)}(\omega)$ , dashed) near-fields for devices with a 240 nm height to the calculated incident laser signal ( $\tilde{E}_S(\omega)$ , dotted). This on-resonant 240 nm device shows two peaks present in the cross-correlation data, one corresponding to the output laser spectrum (at 218 THz) and the other to the plasmonic enhancement of the antenna (at 257 THz).

1 minated 10-15 nanoantennas at a time, the measurements we show are an averaged trace, with all antennas  
 2 contributing simultaneously to the detected current. Beyond these limitations, one must also take into ac-  
 3 count the intensity of  $E_S(t)$ . If comparatively strong, approximately three orders of magnitude below  $E_D(t)$   
 4 and higher, nonlinear distortions will form, degrading the accuracy of the small-signal model. Finally, if the  
 5 signal pulse reaches photon energies higher than the work function of the emitter, linear photoemission due  
 6 to single-photon absorption will cause a substantial background current placing an upper frequency limit of  
 7 a gold device near 1 PHz.

8 Our detection scheme can be directly compared to hetero- and homodyne methods that are often used  
 9 in techniques such as frequency-comb spectroscopy<sup>35-37</sup>. However, the energy detectors used for het-  
 10 ero/homodyne detection do not provide sub-cycle gating and only allow for a narrow detection bandwidth  
 11 that is confined to the amplitude spectrum of the local oscillator (*i.e.* the driver pulse). The sub-cycle gating  
 12 and thus broadband response of the nonlinear nanoantenna detectors enables simultaneous tracking of linear  
 13 and nonlinear light-matter interaction dynamics. The reduced pulse energy requirements and compact form-  
 14 factor of on-chip nanoantenna detectors like those presented in this work could thus be used to enhance the  
 15 performance of emerging frequency-comb spectroscopy systems<sup>38</sup>.

## 1 **Conclusion**

2 While other direct time-domain optical sampling techniques for visible and near-infrared optical pulses  
3 currently exist<sup>10,12–15,17</sup>, they require  $\mu\text{J}$ - to  $\text{mJ}$ -level pulse energies, bulky apparatus, and/or vacuum enclo-  
4 sures. By providing a compact, chip-scale platform that enables sub-cycle, field-sensitive detection of sub-  
5 to few-fJ optical waveforms in ambient conditions, devices similar to those discussed in this work could find  
6 applications such as phase-resolved spectroscopy and imaging, and could have an impact in a variety of fields  
7 such as biology, medicine, food-safety, gas sensing, and drug discovery. In particular, due to their compact  
8 footprint and pJ-level energy requirements, such detectors could be used to enhance the performance and  
9 operating bandwidth of frequency comb spectroscopy systems. We also believe that such on-chip petahertz  
10 field-sampling devices will enable many fundamental scientific investigations such as the time-domain char-  
11 acterization of attosecond electron dynamics and optical-field-driven nonlinear phenomena in light-matter  
12 interactions.

## 13 **Methods**

### 14 *Experimental Methods*

15 The nanodevices were illuminated by a few-cycle, supercontinuum-based<sup>39</sup>, CEP-stabilized fiber laser  
16 source<sup>33</sup>. The source has a central wavelength of  $\sim 1170$  nm, with a pulse duration of  $\sim 10$  fs FWHM  
17 ( $\sim 2.5$  cycles), and repetition rate of 78 MHz. The supercontinuum was generated from a highly non-linear  
18 germanosilicate fiber pumped by a Er: fiber-based laser oscillator and Er-doped fiber amplifier (EDFA) sys-  
19 tem and compressed with a SF10 prism compressor. The CEP was locked to a fixed CEP value for all  
20 measurements taken. Pulse characterization of the laser source was performed by 2DSI<sup>40</sup> and can be found  
21 in Sec. S6. The spectrum of the laser source was measured with a fiber-coupled optical spectrum analyzer  
22 (Ando Electric Co., Ltd.). More details about the supercontinuum source can be found in Ref. [33].

23 A dispersion-balanced Mach-Zehnder interferometer was used to generate the pulse pairs for the exper-  
24 iment. An Inconel reflective neutral density (ND) filter of optical density (OD) 4 on a 2 mm thick BK7  
25 substrate (Thorlabs) was placed in one arm and used to generate a weak signal pulse with pulse energy of  
26  $\sim 5$  fJ. An optical chopper was placed in this weak arm for lock-in detection and amplification. The strong,  
27 driver arm had a pulse energy of  $\sim 50$  pJ. A corresponding 2 mm thick BK7 window was placed in the driver  
28 arm to balance the dispersion between arms. The added chirp from the glass was precompensated using the

1 prism compressor. The delay between the two pulses was controlled with a home built  $15\ \mu\text{m}$  piezo stage.  
2 A chopper was placed in the weak arm to modulate the signal for lock-in amplification. A schematic of  
3 experimental setup can be found in Supplementary Information Fig. S1.

4 The pulses were focused onto the chip using a Cassegrain reflector to a spot-size of  $2.25\ \mu\text{m} \times$   
5  $4.2\ \mu\text{m}$  FWHM. This spot-size allowed for illumination of 10-15 nanoantennas at a time. The polariza-  
6 tion of the pulses was parallel to the nanoantenna height axis (Fig. 1A). A bias voltage of 3 V was applied  
7 across the 50 nm device gap. The emitted current was collected and amplified by a transimpedance amplifier  
8 (FEMTO Messtechnik GmbH) in conjunction with a lock-in amplifier (Stanford Research Systems), with a  
9 modulation of 200 Hz of the optical chopper.

10 For each data set, 60 scans of 10 second acquisition time over the 100 fs time window were performed.  
11 Post-processing was done in Matlab. Each data set was Fourier transformed and windowed from 150 THz to  
12 350 THz with a tukey-window steepness of  $\alpha = 0.2$ . The resulting output was averaged in the time-domain.

### 13 *Device Fabrication*

14 We used a fabrication process based on that described in Ref. [27]. The data presented in this work comes  
15 from devices fabricated on two different chips. The devices were fabricated on BK7 substrates. The pat-  
16 terning was performed using an electron beam lithography process with PMMA A2 resist (Microchem),  
17 a writing current of 2 nA, a dose of  $5000\ \mu\text{C cm}^{-2}$ , and an electron beam energy of 125 keV. To avoid  
18 charging, an Electra92 layer was spin-coated on top of the PMMA at 2 krpm and baked for 2 min at  $90\ ^\circ\text{C}$ .  
19 Since these are large arrays, a proximity effect correction step was also included when designing the layout.  
20 After exposure, the resist was cold-developed in a 3:1 isopropyl alcohol to methyl isobutyl ketone solution  
21 for 60 s at  $0\ ^\circ\text{C}$ . Then, a 2 nm adhesion layer followed by 20 nm of Au were deposited using electron beam  
22 evaporation. An adhesion layer of Ti was used for the 240 nm and Cr for the 200 nm antennas chips. Subse-  
23 quently a liftoff process in a  $65\ ^\circ\text{C}$  bath of n-methylpyrrolidone (NMP) (Microchem) was used to release the  
24 structures. Finally, we used a photolithography procedure to fabricate the contact pads for external electrical  
25 connections.

### 26 *Electromagnetic Simulations*

27 The optical response of the plasmonic nanoantennas was simulated in a finite-element-method electromag-  
28 netic solver (COMSOL Multiphysics). The nanoantenna geometry was extracted from SEM images. The

1 refractive index of gold was taken from Ref. [41], and the refractive index of the glass substrate was fixed  
2 at 1.5 with negligible dispersion in the simulation spectral range. To simulate nanoantenna arrays, periodic  
3 boundary conditions were used. The normally incident plane wave was polarized along the nanotriangle  
4 axis (perpendicular to the nanowire). Perfectly matched layers were used to avoid spurious reflections at  
5 the simulation domain boundaries. The complex field response  $\tilde{H}_{\text{Pl.}}(\omega) = \tilde{E}^{(L)}(\omega)/\tilde{E}(\omega)$  was evaluated as  
6 a function of frequency. The field enhancement was defined as the ratio of the near-field at the nanotriangle  
7 tip to the incident optical field.

### 8 **Data and Code Availability**

9 All data and code is available in the following github repository: [https://github.com/qnngroup/On-chip-](https://github.com/qnngroup/On-chip-sampling-of-optical-fields-with-attosecond-resolution—Data-Analysis)  
10 [sampling-of-optical-fields-with-attosecond-resolution—Data-Analysis](https://github.com/qnngroup/On-chip-sampling-of-optical-fields-with-attosecond-resolution—Data-Analysis).

### 11 **References**

- 12 <sup>1</sup>M. Tonouchi, “Cutting-edge terahertz technology”, *Nat. Photon.*, 97 (2007).
- 13 <sup>2</sup>J. Neu and C. A. Schmuttenmaer, “Tutorial: An introduction to terahertz time domain spectroscopy (THz-  
14 TDS)”, *J. App. Phys.* **124**, 231101 (2018).
- 15 <sup>3</sup>A. Bonvalet, J. Nagle, V. Berger, A. Migus, J.-L. Martin, and M. Joffre, “Femtosecond infrared emission  
16 resulting from coherent charge oscillations in quantum wells”, *Phys. Rev. Lett.* **76**, 4392–4395 (1996).
- 17 <sup>4</sup>O. Schubert, M. Hohenleutner, F. Langer, B. Urbanek, C. Lange, U. Huttner, D. Golde, T. Meier, M. Kira,  
18 S. W. Koch, and R. Huber, “Sub-cycle control of terahertz high-harmonic generation by dynamical Bloch  
19 oscillations”, *Nat. Photon.* **8**, 119–123 (2014).
- 20 <sup>5</sup>C. Riek, D. V. Seletskiy, A. S. Moskalenko, J. F. Schmidt, P. Krauspe, S. Eckart, S. Eggert, G. Burkard, and  
21 A. Leitenstorfer, “Direct sampling of electric-field vacuum fluctuations”, *Science* **350**, 420–423 (2015).
- 22 <sup>6</sup>M. Hohenleutner, F. Langer, O. Schubert, M. Knorr, U. Huttner, S. W. Koch, M. Kira, and R. Huber,  
23 “Real-time observation of interfering crystal electrons in high-harmonic generation”, *Nature* **523**, 572–  
24 575 (2015).
- 25 <sup>7</sup>F. Lépine, M. Y. Ivanov, and M. J. J. Vrakking, “Attosecond molecular dynamics: fact or fiction?”, *Nat.*  
26 *Photon.* **8**, 195–204 (2014).

- 1 <sup>8</sup>M. Schultze, E. M. Bothschafter, A. Sommer, S. Holzner, W. Schweinberger, M. Fiess, M. Hofstetter, R.  
2 Kienberger, V. Apalkov, V. S. Yakovlev, M. I. Stockman, and F. Krausz, “Controlling dielectrics with the  
3 electric field of light”, [Nature](#) **493**, 75–78 (2013).
- 4 <sup>9</sup>A. Schiffrin, T. Paasch-Colberg, N. Karpowicz, V. Apalkov, D. Gerster, S. Mühlbrandt, M. Korbman,  
5 J. Reichert, M. Schultze, S. Holzner, J. V. Barth, R. Kienberger, R. Ernstorfer, V. S. Yakovlev, M. I.  
6 Stockman, and F. Krausz, “Optical-field-induced current in dielectrics”, [Nature](#) **493**, 70–74 (2013).
- 7 <sup>10</sup>S. Sederberg, D. Zimin, S. Keiber, F. Siegrist, M. S. Wismer, V. S. Yakovlev, I. Floss, C. Lemell, J.  
8 Burgdörfer, M. Schultze, F. Krausz, and N. Karpowicz, “Attosecond optoelectronic field measurement in  
9 solids”, [Nat. Commun.](#) **11**, 430 (2020).
- 10 <sup>11</sup>I. Pupeza, M. Huber, M. Trubetskov, W. Schweinberger, S. A. Hussain, C. Hofer, K. Fritsch, M. Poetzl-  
11 berger, L. Vamos, E. Fill, T. Amotchkina, K. V. Kepesidis, A. Apolonski, N. Karpowicz, V. Pervak, O.  
12 Pronin, F. Fleischmann, A. Azzee, M. Žigman, and F. Krausz, “Field-resolved infrared spectroscopy of  
13 biological systems”, [Nature](#) **577**, 52–59 (2020).
- 14 <sup>12</sup>S. B. Park, K. Kim, W. Cho, S. I. Hwang, I. Ivanov, C. H. Nam, and K. T. Kim, “Direct sampling of a light  
15 wave in air”, [Optica](#) **5**, 402 (2018).
- 16 <sup>13</sup>W. Cho, S. I. Hwang, C. H. Nam, M. R. Bionta, P. Lassonde, B. E. Schmidt, H. Ibrahim, F. Légaré, and  
17 K. T. Kim, “Temporal characterization of femtosecond laser pulses using tunneling ionization in the UV,  
18 visible, and mid-IR ranges”, [Sci. Rep.](#) **9**, 16067 (2019).
- 19 <sup>14</sup>J. Itatani, F. Quéré, G. L. Yudin, M. Y. Ivanov, F. Krausz, and P. B. Corkum, “Attosecond streak camera”,  
20 [Phys. Rev. Lett.](#) **88**, 173903 (2002).
- 21 <sup>15</sup>R. Kienberger, E. Goulielmakis, M. Uiberacker, A. Baltuska, V. Yakovlev, F. Bammer, A. Scrinzi, T.  
22 Westerwalbesloh, U. Kleineberg, U. Heinzmann, M. Drescher, and F. Krausz, “Atomic transient recorder”,  
23 [Nature](#) **427**, 817–821 (2004).
- 24 <sup>16</sup>G. Sansone, E. Benedetti, F. Calegari, C. Vozzi, L. Avaldi, R. Flammini, L. Poletto, P. Villoresi, C. Altucci,  
25 R. Velotta, S. Stagira, S. De Silvestri, and M. Nisoli, “Isolated single-cycle attosecond pulses”, [Science](#)  
26 **314**, 443 (2006).
- 27 <sup>17</sup>F. Krausz and M. I. Stockman, “Attosecond metrology: from electron capture to future signal processing”,  
28 [Nat. Photon.](#) **8**, 205–213 (2014).

- 1 <sup>18</sup>P. Dombi, Z. Pápa, J. Vogelsang, S. V. Yalunin, M. Sivilis, G. Herink, S. Schäfer, P. Groß, C. Ropers, and  
2 C. Lienau, “Strong-field nano-optics”, *Rev. Mod. Phys.* **92**, 025003 (2020).
- 3 <sup>19</sup>M. Krüger, C. Lemell, G. Wachter, J. Burgdörfer, and P. Hommelhoff, “Attosecond physics phenomena at  
4 nanometric tips”, *J. Phys. B At. Mol. Opt. Phys.* **51**, 172001 (2018).
- 5 <sup>20</sup>J. Schoetz, Z. Wang, E. Pisanty, M. Lewenstein, M. F. Kling, and M. F. Ciappina, “Perspective on Petahertz  
6 Electronics and Attosecond Nanoscopy”, *ACS Photonics* **6**, 3057–3069 (2019).
- 7 <sup>21</sup>M. F. Ciappina, J. A. Pérez-Hernández, A. S. Landsman, W. A. Okell, S. Zherebtsov, B. Förg, J. Schötz,  
8 L. Seiffert, T. Fennel, T. Shaaran, T. Zimmermann, A. Chacón, R. Guichard, A. Zaïr, J. W. Tisch, J. P.  
9 Marangos, T. Witting, A. Braun, S. A. Maier, L. Roso, M. Krüger, P. Hommelhoff, M. F. Kling, F. Krausz,  
10 and M. Lewenstein, “Attosecond physics at the nanoscale”, *Reports Prog. Phys.* **80**, 054401 (2017).
- 11 <sup>22</sup>M. I. Stockman, K. Kneipp, S. I. Bozhevolnyi, S. Saha, A. Dutta, J. Ndukaife, N. Kinsey, H. Reddy, U.  
12 Guler, V. M. Shalaev, A. Boltasseva, B. Gholipour, H. N. Krishnamoorthy, K. F. Macdonald, C. Soci,  
13 N. I. Zheludev, V. Savinov, R. Singh, P. Groß, C. Lienau, M. Vadai, M. L. Solomon, D. R. Barton, M.  
14 Lawrence, J. A. Dionne, S. V. Boriskina, R. Esteban, J. Aizpurua, X. Zhang, S. Yang, D. Wang, W. Wang,  
15 T. W. Odom, N. Accanto, P. M. De Roque, I. M. Hancu, L. Piatkowski, N. F. Van Hulst, and M. F. Kling,  
16 “Roadmap on plasmonics”, *J. Opt.* **20**, 043001 (2018).
- 17 <sup>23</sup>M. Ludwig, G. Aguirregabiria, F. Ritzkowski, T. Rybka, D. C. Marinica, J. Aizpurua, A. G. Borisov,  
18 A. Leitenstorfer, and D. Brida, “Sub-femtosecond electron transport in a nanoscale gap”, *Nat. Phys.* **16**,  
19 341–345 (2020).
- 20 <sup>24</sup>W. P. Putnam, R. G. Hobbs, P. D. Keathley, K. K. Berggren, and F. X. Kärtner, “Optical-field-controlled  
21 photoemission from plasmonic nanoparticles”, *Nat. Phys.* **13**, 335–339 (2017).
- 22 <sup>25</sup>P. D. Keathley, W. P. Putnam, P. Vasireddy, R. G. Hobbs, Y. Yang, K. K. Berggren, and F. X. Kärt-  
23 ner, “Vanishing carrier-envelope-phase-sensitive response in optical-field photoemission from plasmonic  
24 nanoantennas”, *Nat. Phys.* **15**, 1128 (2019).
- 25 <sup>26</sup>M. Krüger, M. Schenk, and P. Hommelhoff, “Attosecond control of electrons emitted from a nanoscale  
26 metal tip”, *Nature* **475**, 78–81 (2011).

- 1 <sup>27</sup>Y. Yang, M. Turchetti, P. Vasireddy, W. P. Putnam, O. Karnbach, A. Nardi, F. X. Kärtner, K. K. Berggren,  
2 and P. D. Keathley, “Light Phase Detection with On-Chip Petahertz Electronic Networks”, *Nat. Commun.*  
3 **11**, 3407 (2020).
- 4 <sup>28</sup>M. Ludwig, A. K. Kazansky, G. Aguirregabiria, D. C. Marinica, M. Falk, A. Leitenstorfer, D. Brida, J.  
5 Aizpurua, and A. G. Borisov, “Active control of ultrafast electron dynamics in plasmonic gaps using an  
6 applied bias”, *Phys. Rev. B* **101**, 241412 (2020).
- 7 <sup>29</sup>R. Gomer, *Field emission and field ionization*, Vol. 34 (Harvard University Press Cambridge, MA, 1961).
- 8 <sup>30</sup>T. Rybka, M. Ludwig, M. F. Schmalz, V. Knittel, D. Brida, and A. Leitenstorfer, “Sub-cycle optical phase  
9 control of nanotunnelling in the single-electron regime”, *Nat. Photon.* **10**, 667–670 (2016).
- 10 <sup>31</sup>R. H. Fowler and L. Nordheim, “Electron Emission in Intense Electric Fields”, *Proc. R. Soc. A* **119**, 173–  
11 **181** (1928).
- 12 <sup>32</sup>F. V. Bunkin and M. V. Fedorov, “Cold Emission of Electrons from Surface of a Metal in a Strong Radia-  
13 tion Field”, *Soviet Physics JETP* **21**, 896–899 (1965).
- 14 <sup>33</sup>W. P. Putnam, P. D. Keathley, J. A. Cox, A. Liehl, A. Leitenstorfer, and F. X. Kärtner, “Few-cycle,  
15 carrier-envelope-phase-stable laser pulses from a compact supercontinuum source”, *J. Opt. Soc. Am. B*  
16 **36**, A93 (2019).
- 17 <sup>34</sup>A. Anderson, K. S. Deryckx, X. G. Xu, G. Steinmeyer, and M. B. Raschke, “Few-Femtosecond Plas-  
18 mon Dephasing of a Single Metallic Nanostructure from Optical Response Function Reconstruction by  
19 Interferometric Frequency Resolved Optical Gating”, *Nano Lett.* **10**, 2519–2524 (2010).
- 20 <sup>35</sup>N. Picqué and T. W. Hänsch, “Frequency comb spectroscopy”, *Nat. Photon.* **13**, 146–157 (2019).
- 21 <sup>36</sup>I. Coddington, W. C. Swann, and N. R. Newbury, “Coherent multiheterodyne spectroscopy using stabi-  
22 lized optical frequency combs”, *Phys. Rev. Lett.* **100**, 013902 (2008).
- 23 <sup>37</sup>B. J. Bjork, T. Q. Bui, O. H. Heckl, P. B. Changala, B. Spaun, P. Heu, D. Follman, C. Deutsch, G. D. Cole,  
24 M. Aspelmeyer, M. Okumura, and J. Ye, “Direct frequency comb measurement of OD + CO → DOCO  
25 kinetics”, *Science* **354**, 444–448 (2016).
- 26 <sup>38</sup>A. S. Kowligy, H. Timmers, A. J. Lind, U. Elu, F. C. Cruz, P. G. Schunemann, J. Biegert, and S. A.  
27 Diddams, “Infrared electric field sampled frequency comb spectroscopy”, *Sci. Adv.* **5**, eaaw8794 (2019).

- 1 <sup>39</sup>A. Sell, G. Krauss, R. Scheu, R. Huber, and A. Leitenstorfer, “8-fs pulses from a compact er:fiber system:  
2 quantitative modeling and experimental implementation”, *Opt. Express* **17**, 1070–1077 (2009).
- 3 <sup>40</sup>J. R. Birge, R. Ell, and F. X. Kärtner, “Two-dimensional spectral shearing interferometry for few-cycle  
4 pulse characterization”, *Opt. Lett.* **31**, 2063 (2006).
- 5 <sup>41</sup>P. B. Johnson and R. W. Christy, “Optical constants of the noble metals”, *Phys. Rev. B* **6**, 4370–4379  
6 (1972).

## 7 **Acknowledgements**

8 This material is based upon work supported by the Air Force Office of Scientific Research under award  
9 numbers FA9550-19-1-0065 and FA9550-18-1-0436. F.X.K. acknowledges support by the European Re-  
10 search Council under the European Union’s Seventh Framework Programme (FP7/2007–2013) through the  
11 Synergy Grant ‘Frontiers in Attosecond X-ray Science: Imaging and Spectroscopy’ (AXSIS) (609920) and  
12 by the Cluster of Excellence ‘CUI: Advanced Imaging of Matter’ of the Deutsche Forschungsgemeinschaft  
13 (DFG) - EXC 2056 - project ID 390715994. This work was also partially supported by a seed grant pro-  
14 vided by SENSE.nano, a center of excellence powered by MIT.nano, as well as the PIER Hamburg – MIT  
15 Program. We thank Marco Colangelo and John Simonaitis for their scientific discussion and edits to the  
16 manuscript. We thank Navid Abedzadeh for taking photos of the chip.

## 17 **Author Contributions**

18 F.R., M.R.B. and P.D.K., conceived the experiments. Y.Y. and D.C.M. simulated the optical response of  
19 the devices. M.T. fabricated the devices. M.R.B., F.R., and M.T. performed the experiments with assistance  
20 from P.D.K. F.R. derived the theory and simulated the results with input from P.D.K., M.R.B., and W.P.P.  
21 F.R. and M.R.B. analyzed the data with input from P.D.K., W.P.P., M.T., and Y.Y. M.R.B. and F.R. wrote  
22 the first draft of the manuscript and Supplementary Information with significant contributions from M.T.,  
23 Y.Y., P.D.K., and W.P.P. K.K.B. and F.X.K. provided input and feedback throughout the process. All authors  
24 contributed to the writing and editing of the manuscript.

## 25 **Competing Interests**

26 The authors declare a patent application has been filed based on the devices described in this manuscript.

# Figures

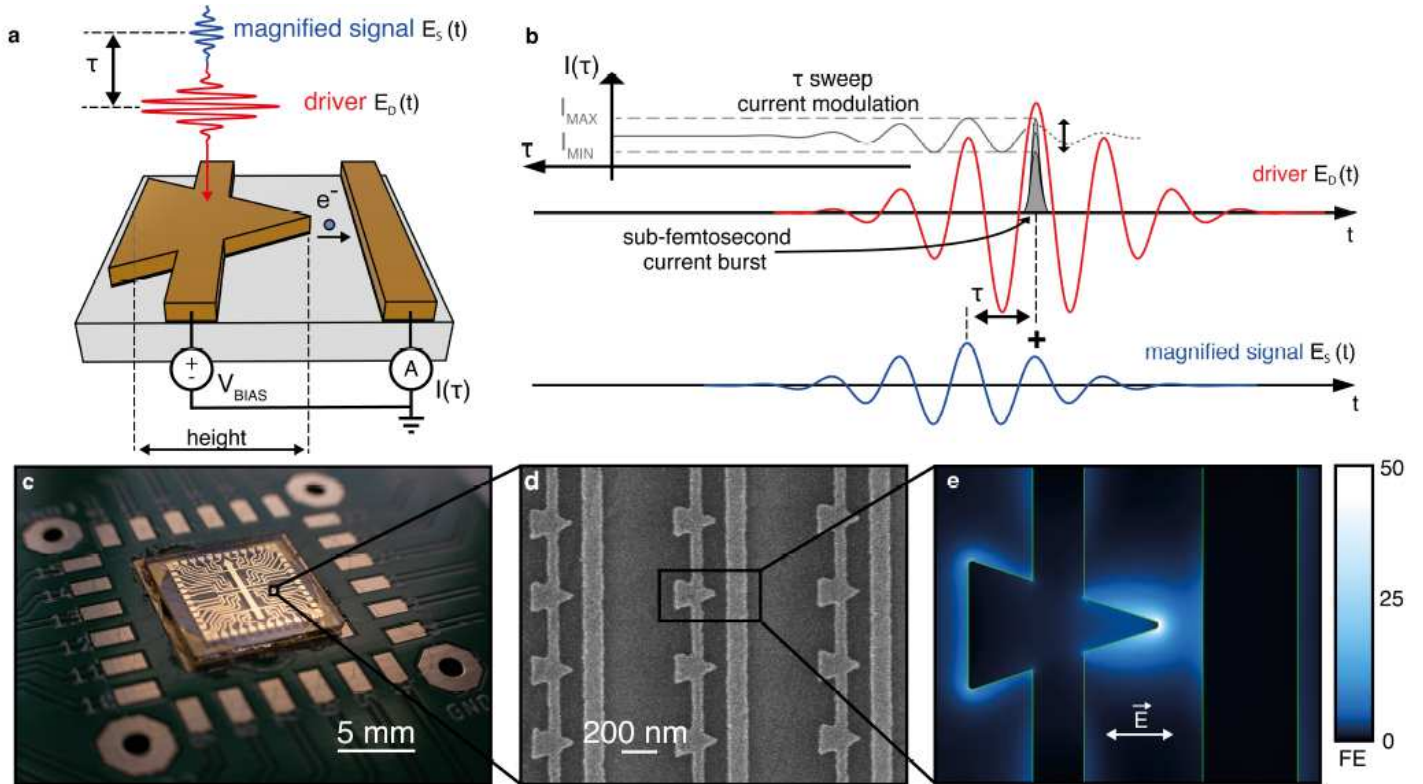


**Figure 1**

Device overview. a, Schematic of the device. b, Depiction of the optical-field sampling process. Attosecond electron bursts are driven from an electrically-connected gold nanoantenna (see a) by a strong optical waveform driver ( $E_D(t)$ , red), collected by an adjacent gold wire, then measured using an external current detector (see Methods). The weak signal waveform ( $E_S(t)$ , blue), with a peak intensity of  $1 \times 10^{-4}$  that of the driver pulses, modulates the average photocurrent generated by the driver pulse,  $I(t)$ , as a function of delay,  $t$  (grey). The amplitude of the signal waveform is artificially magnified in a and b for visibility. c, Photograph of the nanocircuit embedded on printed circuit board. d, Scanning electron micrograph of the device. e, Simulated electric field enhancement around a nanoantenna. The maximum field enhancement is  $\sim 35$ . FE: field enhancement factor. E: polarization direction of the incident electric field.

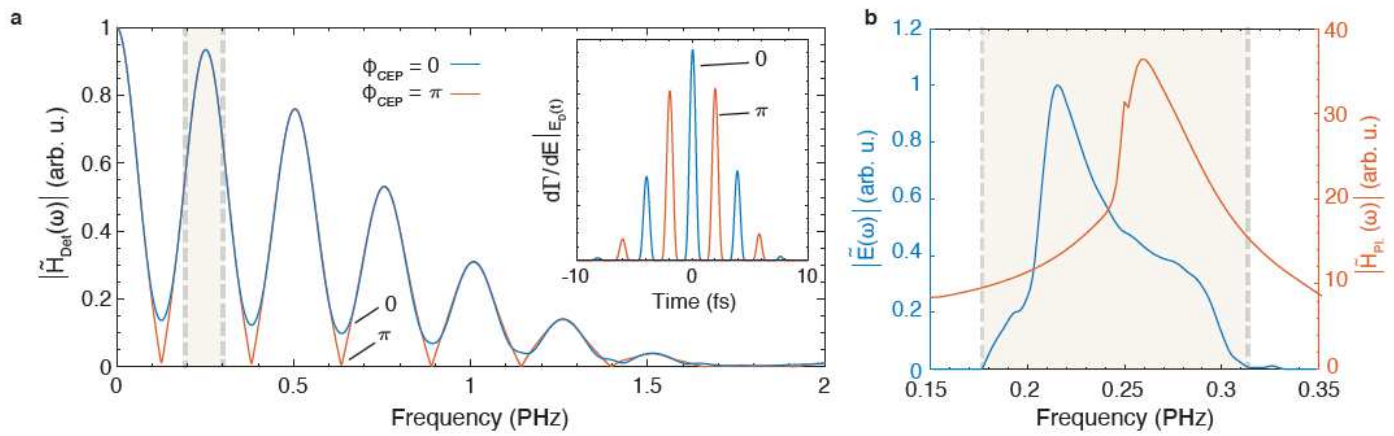


**Figure 2**

Theoretical sampling bandwidth. a, Calculation of the accessible sampling bandwidth  $|\tilde{H}_{\text{Det}}(\omega)|$  for the carrier-envelope phases  $\phi_{\text{CEP}} = 0, \pi$  of the driver pulse (blue and red respectively). (Inset) The time-domain picture of  $d\Gamma/dE|E_d(t)|$  corresponding to the bandwidth shown in a. b, The spectral amplitude of the driving pulse ( $E_d(t)$ , blue) and the plasmonic nanoantenna transfer function  $|\tilde{H}_{\text{PI}}(\omega)|$  (red). The shaded area in a and b indicates the spectral region occupied by the driving pulse.

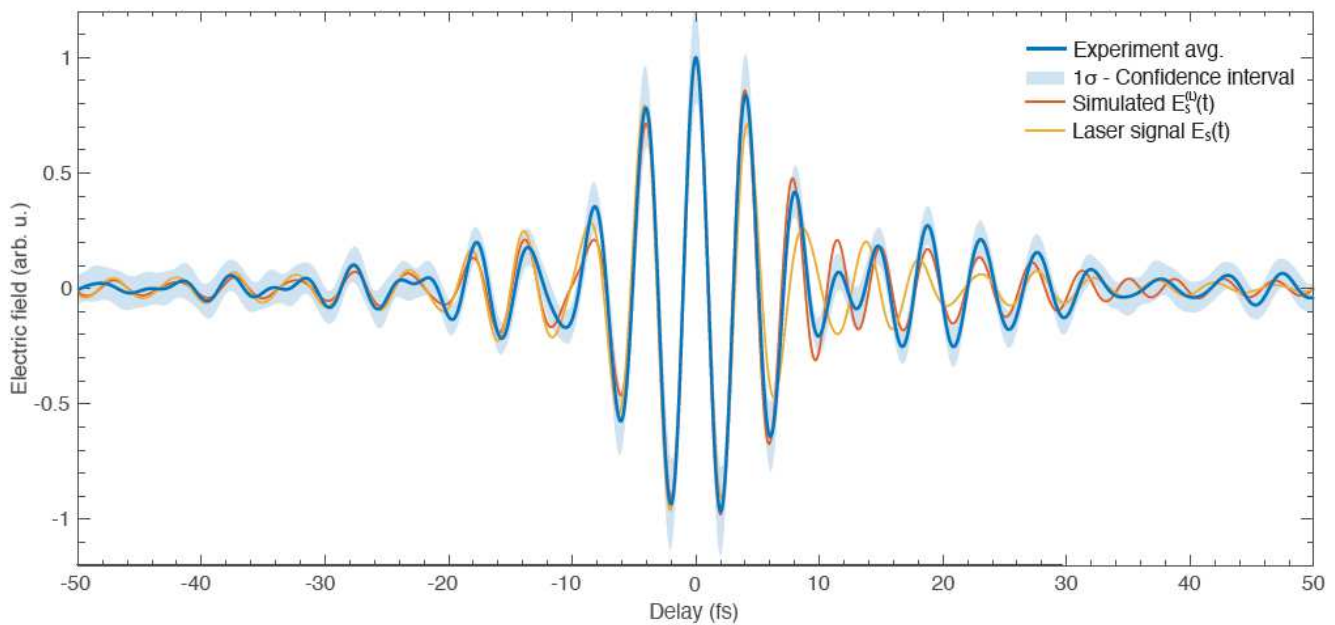


**Figure 3**

Experimental field sampling results and analysis. Time-domain results for devices with a height of 240 nm comparing measured (blue) and simulated near-fields ( $E(L)$  S (t), red) to the calculated incident laser signal ( $E_S(t)$ , yellow). Negative delays indicate that the driver pulse arrives before the signal pulse. The 1s-confidence interval is shown as a blue shaded ribbon centered around the average value (blue solid

line) retrieved from 60 scans. The plasmonic resonance of the antenna results in the dephasing in the time-domain between  $E_S(t)$  and  $E(L) S(t)$  observed around 12 fs.

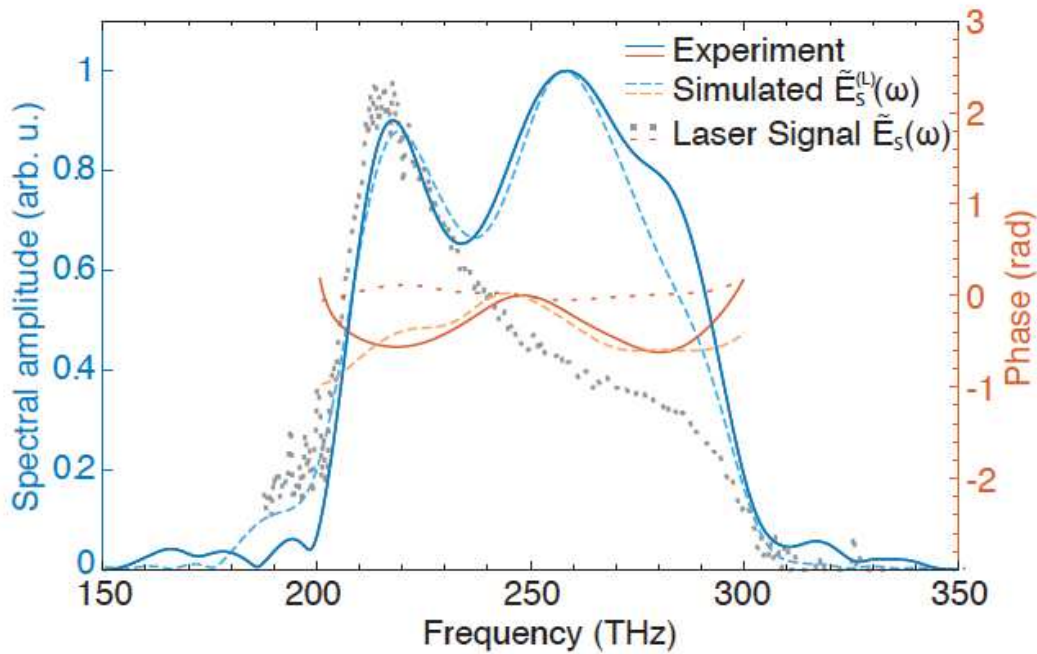


**Figure 4**

Frequency-domain of the experimental field sampling results Frequency-domain comparison of measured (solid) and simulated ( $\tilde{E}^{(L)} S(\omega)$ , dashed) near-fields for devices with a 240 nm height to the calculated incident laser signal ( $\tilde{E}_S(\omega)$ , dotted). This on-resonant 240 nm device shows two peaks present in the cross-correlation data, one corresponding to the output laser spectrum (at 218 THz) and the other to the plasmonic enhancement of the antenna (at 257 THz).

## Supplementary Files

This is a list of supplementary files associated with this preprint. Click to download.

- [SamplerpaperSI.pdf](#)